

RESEARCH

Open Access



S-adenosylmethionine metabolism shapes CD8⁺ T cell functions in colorectal cancer

Xiaohua Yang¹, Tianzhang Kou^{1,2}, Hongmiao Wang^{1,2}, Ji Zhu^{3,4}, Zheng-Jiang Zhu^{1,5} and Yuping Cai^{1*}

Abstract

Metabolite nutrients within the tumor microenvironment shape both tumor progression and immune cell functionality. It remains elusive how the metabolic interaction between T cells and tumor cells results in different anti-cancer immunotherapeutic responses. Here, we use untargeted metabolomics to investigate the metabolic heterogeneity in patients with colorectal cancer (CRC). Our analysis reveals enhanced S-adenosylmethionine (SAM) and S-adenosylhomocysteine (SAH) metabolism in microsatellite stable (MSS) CRC, a subtype known for its resistance to immunotherapy. Functional studies reveal that SAM and SAH enhance the initial activation and effector functions of CD8⁺ T cells. Instead, cancer cells outcompete CD8⁺ T cells for SAM and SAH availability to impair T cell survival. In vivo, SAM supplementation promotes T cell proliferation and reduces exhaustion of the tumor-infiltrating CD8⁺ T cells, thus suppressing tumor growth in tumor-bearing mice. This study uncovers the metabolic crosstalk between T cells and tumor cells, which drives the development of tumors resistant to immunotherapy.

Keywords Metabolite nutrients, CD8⁺ T cell function, Microsatellite stable colorectal cancer, Metabolomics, S-adenosylmethionine (SAM) and S-adenosylhomocysteine (SAH) metabolism

Introduction

Colorectal cancer (CRC) is a leading cause of cancer-related deaths, accounting for nearly one million annual deaths in recent years. Colorectal cancer can be classified into proficient mismatch repair (pMMR)/microsatellite stability (MSS) and mismatch repair deficiency (dMMR)/microsatellite instability (MSI) according to the stability

of the tumor genome [1, 2]. MSI CRC with a high tumor mutation burden presents an inflammatory tumor microenvironment of tumor infiltrating lymphocytes (TILs) such as cytotoxic T cells [2, 3]. This lends benefits to patients with MSI CRC who are usually responsive to treatments based on immune checkpoint blockade such as programmed death-ligand 1 (PD-L1) inhibitors in clinic [4]. However, MSS CRC, which is as high as 85% of all CRCs, is highly insensitive to immune checkpoint blockade, and is refractory to immunotherapies [4, 5]. Thus, there is a sizeable unmet need to improve therapeutic care for patients with MSS CRC.

Both tumor progression and anti-tumor immune responses are shaped by metabolite nutrients within the tumor microenvironment [6, 7]. As an essential niche, the availability of metabolite nutrients significantly impacts the proliferation of tumor cells and the survival and function of immune cells [8–10]. Tumor cells are

*Correspondence:

Yuping Cai
yupingcai@sioc.ac.cn

¹Interdisciplinary Research Center on Biology and Chemistry, Shanghai Institute of Organic Chemistry, Chinese Academy of Sciences, Shanghai 200032, China

²University of Chinese Academy of Sciences, Beijing 100049, China

³Department of Radiation Oncology, Zhejiang Cancer Hospital, Hangzhou 310000, China

⁴Hangzhou Institute of Medicine (HIM), Chinese Academy of Sciences, Hangzhou 310000, China

⁵Shanghai Key Laboratory of Aging Studies, Shanghai 201210, China



© The Author(s) 2025. **Open Access** This article is licensed under a Creative Commons Attribution-NonCommercial-NoDerivatives 4.0 International License, which permits any non-commercial use, sharing, distribution and reproduction in any medium or format, as long as you give appropriate credit to the original author(s) and the source, provide a link to the Creative Commons licence, and indicate if you modified the licensed material. You do not have permission under this licence to share adapted material derived from this article or parts of it. The images or other third party material in this article are included in the article's Creative Commons licence, unless indicated otherwise in a credit line to the material. If material is not included in the article's Creative Commons licence and your intended use is not permitted by statutory regulation or exceeds the permitted use, you will need to obtain permission directly from the copyright holder. To view a copy of this licence, visit <http://creativecommons.org/licenses/by-nc-nd/4.0/>.

highly metabolically active with enhanced glycolysis, amino acid metabolism and lipid synthesis to fuel proliferation, leading to a rapid consumption of nutrients in the microenvironment [11, 12]. Likewise, immune cells require metabolite nutrients to exert essential anti-tumor immune functions [13–15]. For example, arginine regulates immune responses and improves anti-tumor activity of CD8⁺ T cells. However, most tumor cells consume large amounts of extrinsic arginine in the tumor microenvironment due to a lack of argininosuccinate synthase 1 (ASS1), thereby inhibiting the activation of anti-tumor immune cells [16]. Metabolic intervention through increasing intratumoural arginine levels has marked synergistic effects with PD-L1 blocking antibodies on tumor immunotherapy [16, 17]. Bian et al., recently reported that tumor methionine consumption is an immune evasion mechanism by which cancer cells outcompete T cells for methionine and impair T cell immunity in mouse bearing with CRC tumor [18]. These compelling findings increasingly appreciate metabolite nutrients as key mediators simultaneously regulating both tumor cells and immune cells, which leaves ample potential of applying metabolic modulation for cancer immunotherapy [19, 20].

Metabolomics enables to simultaneously measure hundreds to thousands of metabolites and offers molecular insights towards pathological phenotypes [21–23]. The metabolism of colorectal cancer has been overwhelmingly studied using metabolomic profiling to analyze specimen collected from patients with CRC [24–27]. However, the tumor-intrinsic metabolic heterogeneity between patients with MSS and MSI CRCs has remained virtually unexplored. More importantly, it is not known the metabolic interactions between immune and tumor cells, and how the metabolism leads to differences in immune responses between the two types of CRC tumors. In this work, to characterize metabolic heterogeneity between MSS and MSI CRCs, we performed comprehensive metabolomic profiling on primary tumors ($n=40$) and paired adjacent normal tissues ($n=40$) from CRC patients, revealing distinctive metabolic portraits between the two patient groups. In particular, we discovered that MSS and MSI CRCs differ in S-adenosylmethionine (SAM)/S-adenosylhomocysteine (SAH) metabolism, as well as T cell signatures in an independent cohort. We further demonstrated that both SAM and SAH enhance the initial activation and effector function of CD8⁺ T cells. Instead, colon cancer cells outcompete CD8⁺ T cells for SAM and SAH availability to impair T cell survival in vitro. In vivo, we demonstrated that SAM supplementation promotes T cell proliferation and reduces exhaustion of the tumor-infiltrating CD8⁺ T cells, with a result of suppressed tumor growth in the CT26 tumor-bearing mice. These findings provide new

insights into the metabolic heterogeneity in CRC and highlight SAM metabolism as potential immunotherapeutic targets for MSS CRC.

Methods

Patients

We collected primary tumors and paired adjacent normal tissues from patients with colorectal cancer ($n=40$) diagnosed from Zhejiang Cancer Hospital (ZJCH, Zhejiang, China). All of the patients were staged according to the Union for International Cancer Control (UICC) pathologic tumor-node-metastasis (TNM) classification system (eighth edition, 2016). The sample collection protocol was approved by the Ethics Committee of the Zhejiang Cancer Hospital (ZJCH, Zhejiang, China) and written informed consent was obtained from the patients enrolled in this study.

Mice

Six-week-old male C57BL/6 and BALB/c mice were ordered from Beijing Vital River Laboratory Animal Technology Co. Ltd. All mice were maintained under SPF housing. Animal studies were conducted under the approval of the ethical guidelines of the Institutional Animal Care and Use Committees of the Shanghai Origin RBH Co., Ltd. (approved project number: SOP-MAE-006-027).

Cell lines

CT26 cells were cultured in DMEM containing 10% FBS and antibiotics (100 U/mL penicillin and 100 µg/mL streptomycin). CT26 (RRID: CVCL_7256) cell line was obtained from the Cell bank of the Chinese Academy of Sciences. Cells were tested negative for mycoplasma contamination.

Tumor model

We established CT26 tumors and mice were inoculated subcutaneously with 1×10^6 CT26 cells. 6 days after tumor establishment, the mice were randomly divided into three groups and were treated with PBS, or SAM, or SAH through intratumoral administration. The stock solution of SAM and SAH were prepared in PBS with 1% DMSO. The working solution of SAM and SAH were diluted with PBS, and the final concentrations of DMSO were 0.04% and 7.7e-5%, respectively. Mice were administered with ~20 µL solution of resultant SAM ($39.84 \mu\text{g kg}^{-1}$), or SAH ($0.08 \mu\text{g kg}^{-1}$). Given the extremely low proportion of DMSO in the solution, mice in the control group receive only PBS without DMSO. The mice were treated once two days for three consecutive times. Tumors were measured using a calliper at individual time points. Tumor areas were calculated as follows: length \times width. Mice were euthanized by CO₂ and sacrificed on

day13 for flow cytometry and metabolomics analyses. It is noted that CO₂ may have effects on mouse metabolome during process.

Metabolite extraction

20 ± 0.5 mg of each frozen tumor tissue was homogenized with 200 µL H₂O and ceramic beads using a homogenizer (JXFSTPRP-CL, Shanghai Jingxin Experimental Technology) at the low-temperature condition. 200 µL homogenized solution was taken out for each sample and 800 µL extraction solution (ACN: MeOH = 1:1, v/v) was added for metabolite extraction. The mixture solution was vortexed for 30 s, and sonicated for 10 min at 4 °C water bath. Then the sample was incubated for 1 h at -20 °C, followed by centrifugation for 15 min at 16,200 × g and 4 °C. The supernatant was taken to a new 1.5-mL EP tube and evaporated to dryness at 4 °C in a vacuum concentrator. The dry extracts were then reconstituted in 100 µL of ACN: H₂O (1:1, v/v), sonicated for 10 min, and centrifuged at 13,000 rpm (15,000 g) and 4 °C for 15 min to remove insoluble debris. The supernatant was transferred glass vials. A pooled quality control sample was prepared by mixing 5 µL of extracted solution from each sample into a vial. All the vials were capped and stored at -80 °C prior to LC-MS analysis.

For extraction of metabolites in cells, the culture medium was quickly removed, and cells were washed with PBS twice. Cell dishes were placed on dry ice and the metabolite extraction solution (MeOH: ACN: H₂O = 2/2/1, v/v/v, 800 µL) was added to dishes to quench metabolism. The cell contents were scraped and transferred to a 1.5-mL Eppendorf tube. Another 400 µL extraction solution was added to wash dish and transferred to the same EP tube. The samples were vortexed for 1 min and centrifuged for 10 min at 16,200 × g and 4 °C to precipitate insoluble materials. The supernatant was taken to a new 1.5-mL EP tube and evaporated to dryness at 4 °C in a vacuum concentrator. The insoluble debris was further analyzed to and the protein content of each sample was evaluated using the BCA Protein Assay Kit (Thermo Fisher Scientific, Rockford, IL). The volumes of reconstitution solvent for the dry extracts of individual samples were normalized to the BCA assay values.

LC-MS based metabolomic analysis

For untargeted metabolomic profiling, the LC-MS analysis protocol followed that in our previous publication [28]. The data was acquired using a UHPLC system (Vanquish, Thermo Scientific) coupled to an orbitrap mass spectrometer (Exploris 480, Thermo Scientific). A Waters ACQUITY UPLC BEH amide column (particle size, 1.7 µm; 100 mm (length) × 2.1 mm (i.d.)) and Kinetex C18 column (2.6 µm, 2.1 × 100 mm) were used for the LC separation and the column temperature was kept at

25 °C. For amide column, mobile phase A was 25 mM NH₄OH + 25 mM NH₄OAc in water, and B was ACN for both the positive (ESI+) and negative (ESI-) ionization modes. The sample injection volume was 2 µL. Mobile phases, gradient elution for BEH amide column and C18 column followed the previous publication [28]. LC-MS data acquisition was operated under full MS scan polarity switching mode for all samples. A ddMS2 scan was applied for QC samples to acquire MS/MS spectra. ESI source parameters were set as follows: spray voltage, 3500 V or -2800 V, in positive or negative modes, respectively; aux gas heater temperature, 350 °C; sheath gas, 50 arb; aux gas, 15 arb; capillary temperature, 400 °C. The full MS scan was set as: orbitrap resolution, 60,000; AGC target, 1e6; maximum injection time, 100 ms; scan range, 70-1200 Da. The ddMS2 scan was set as: orbitrap resolution, 30,000; AGC target, 1e5; maximum injection time, 60 ms; scan range, 50-1200 Da; top N setting, 6; isolation width, 1.0 m/z; collision energy mode, stepped; collision energy type, normalized; HCD collision energies (%), SNCE 20-30-40%; Dynamic exclusion duration was set as 4 s for excluding after 1 time.

For quantification of SAM and SAH concentration, a BEH Z-HILIC column (particle size, 1.7 µm; 100 mm (length) × 2.1 mm (i.d.)) was used for LC separation. The mobile phases A was 15 mM ammonium bicarbonate in water (pH = 9.0), while mobile phases B was 15 mM ammonium bicarbonate in 90% acetonitrile and 10% water (pH = 9.0) for both ESI positive and negative ionization modes. The linear gradient eluted from 90% B to 65% B (0-5.0 min, 0.5 mL/min), 65% B (5.0-6.0 min, 0.5 mL/min), 65% B to 90% B (6.0-6.5 min, 0.5 mL/min), 90% B (6.5-9.5 min, 1.0 mL/min), 90% B (9.5-9.51 min, 1.0 mL/min). Parameters of ESI source and MS scanning followed the description as described above.

Metabolomics data processing

Untargeted metabolomics data processing followed our previous publications [28-30]. In brief, raw MS data (.raw) files were converted into the mzXML format by ProteoWizard (version 3.0.20360) and processed by XCMS (version 3.2; <https://bioconductor.org/packages/release/bioc/html/xcms.html>) for peak detection, retention time correction, and peak alignment. Metabolite annotation was performed using MetDNA (<http://metdna.zhulab.cn/>) [29, 30]. The metabolite annotation parameters were set as "HILIC" or "RP" according to liquid chromatography mode, and "30" or "SNCE_20_30_40%" for collision energy. Metabolites with level 1 identification were used for statistical analyses.

We used Skyline (version 22.2.0.351) for manual integration of the peak areas of metabolites in cell samples and standard samples for calibration curve. The raw data files (.d) and the *m/z* values, and retention time (RT) of

the target metabolites were imported into Skyline. The target metabolites were manually inspected, and the integration intervals were adjusted.

T cell isolation and activation

Mouse primary CD8⁺ T cells were isolated from the spleens of wildtype C57BL/6 mice using a mouse CD8⁺ T cells isolation kit (StemCell Biotec, Canada). Primary CD8⁺ T cells were cultured 48 h with complete RPMI 1640 medium containing 10% FBS, 100 U mL⁻¹ penicillin, and 100 mg mL⁻¹ streptomycin, 0.05 mM 2-mercaptoethanol and IL-7 (10 ng mL⁻¹). The CD8⁺ T cells were stimulated on plate-bound anti-CD3/CD28 (2 µg mL⁻¹) with IL-2 (10 ng mL⁻¹) for 2 h, 24 h, and 72 h.

The intratumor CD45⁺ tumor-infiltrating leukocytes from BALB/c mice were isolated as follows:

Tumor tissues were cut into pieces (≤ 2 mm) and suspended with 5 mL tumor digestion buffer (500 µL collagenase/hyaluronidase solution, 750 µL 1 mg mL⁻¹ DNase I solution, and 3.75 mL RPMI-1640 medium). After incubation at 37 °C for 1.5 h on a shaking platform, the digested tumor tissues were transferred into a 40-µm mesh nylon strainer on a 50 mL conical tube, pushed through the strainer using the rubber end of a syringe plunger, and rinsed with the recommended medium (PBS containing 2% FBS and 1 mM EDTA.). After centrifugation at 300 x g for 10 min at room temperature, the resulting cell pellets were added with 10 mL of ammonium chloride solution for incubation at room temperature for 5 min, followed by centrifugation at 300 x g for 10 min at room temperature. The resulting cell pellets were re-suspended at 1–10 × 10⁶ cells per mL in PBS and then subjected to CD45⁺ tumor-infiltrating leukocytes isolation by magnetic bead purification using the EasySep Mouse TIL (CD45) Positive Selection Kit according to the manufacturer's instructions (Stemcell Technologies).

CD8⁺ T cell and colon cancer cell coculture assay

Transwell insert chambers with 0.4 µm porous membranes (Corning) were used for non-contact coculture. Mouse primary CD8⁺ T cells were first cultured for 48 h and activated by plate-bound anti-CD3/CD28 antibody for 48 h. CD8⁺ T cells and CT26 cells were then cocultured in a 5:1 ratio for 48 h with 0.2 µM SAH or 100 µM SAM in an incubator at 37 °C with 5% CO₂. CD8⁺ T cells were added to the top chamber and CT26 cells were added to the bottom chamber. Cells in individual chambers were harvested and analyzed by flow cytometry.

Flow cytometry analysis (FACS)

Mouse primary CD8⁺ T cells were stained with eFluor™ 450 anti-mouse CD8a (53–6.7), PE anti-mouse CD69 (H1.2F3), APC anti-mouse CD25 (Clone PC61.5), FITC Anti-mouse CD44 (Clone IM7), PE anti-mouse TNF-α

(MP6-XT22), APC anti-mouse IFN-γ (XMG1.2), and FITC anti-mouse GZMB (NGZB), and FITC-Annexin V mAbs. Intratumor T cells were stained with FITC Anti-mouse CD45 (Clone 30-F11), Brilliant Violet 650 Anti-mouse CD8a (Clone 53–6.7), PE-Cyanine5 Anti-mouse CD4 (Clone GK1.5), PE Anti-mouse Ki-67 (Clone SolA15), APC Anti-mouse FOXP3 (Clone FJK-16s), Brilliant Violet 421 Anti-mouse CD279 (PD-1) (Clone 29 F.1A12), and PE-Cyanine7 Anti-mouse CD366 (TIM3) (Clone RMT3-23).

For surface staining, CD8⁺ T cells were seeded onto plates coated with anti-CD3/CD28. Cells were harvested two hours after seeding and staining with anti-CD69 antibody. Cells were harvested 24 h after seeding and staining with anti-CD25 antibody and anti-CD44 antibody. For intracellular staining, cells were stimulated and Bafilomycin A1 (BFA, 3 µg mL⁻¹) were added during the last 4 h. For IFN-γ, TNF-α and granzyme B analysis, cells were stained with anti-CD8 or anti-CD4 first, then fixed (00-8222-49, eBioscience), permeabilized and stained with Permeabilization Buffer (00-8333-56, eBioscience) according to the manufacturer's protocol. For Ki-67 and FOXP3 analysis, mouse cells were stained with anti-CD8 or anti-CD4 first, then fixed, permeabilized and stained with Transcription Factor Staining Buffer Set (00-5523-00, eBioscience) according to the manufacturer's protocol. For apoptosis staining, cells were harvested, resuspended, and analyzed using an Annexin V Apoptosis Detection Kit (Thermo Fisher Scientific). The apoptosis staining samples were acquired on guava EasyCyte HT (Merck Millipore). Other samples were acquired on Attune NxT Flow Cytometer (Thermo Fisher Scientific). Data analysis was performed using Flowjo software (version 10.3.1).

Quantification and statistical analysis

Data are presented as the mean ± standard error of the mean (SEM) from biological replicates. For untargeted metabolomics analysis of CRC patient cohort, significant differences among four groups were analyzed using One-way analysis of variance (ANOVA). Comparative analysis of two groups was analyzed using two-sided Student's *t*-test, followed by False Discovery Rate (FDR) multiple comparison test using R program. Statistical significance was set at FDR adjusted $P < 0.05$. A broad rule of thumb from previous publications is that 3–10 mice per group are usually used in metabolite-treated immunology experiments to have adequate power, such as flow cytometry analyses or cytokine profiling [18, 31]. Accordingly, $n = 8$ biologically independent animals were used in this study for in vivo experiments in mice.

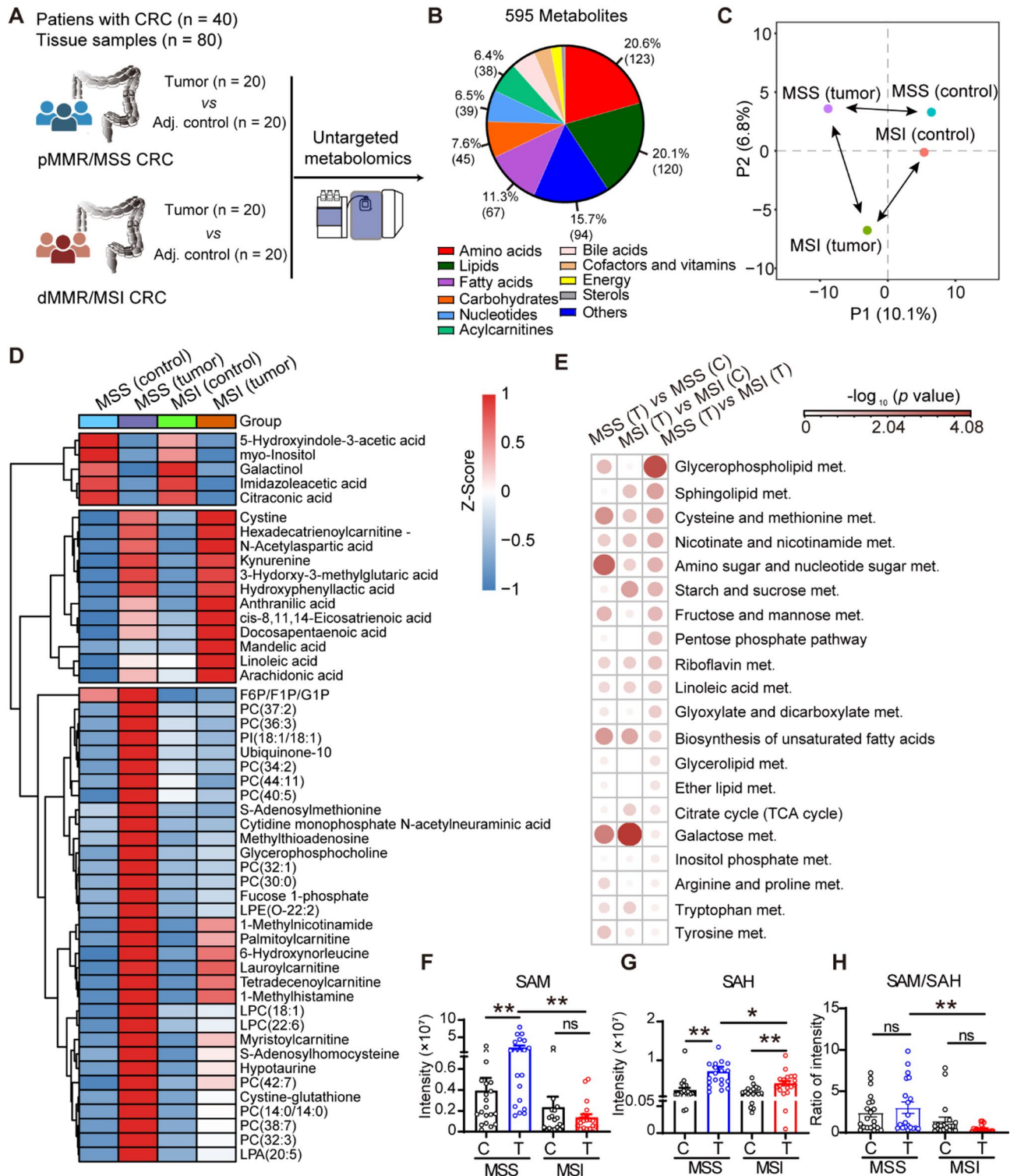


Fig. 1 (See legend on next page.)

Results

Metabolic heterogeneity between MSS and MSI CRCs

To investigate the metabolic differences between MSS and MSI CRCs, we first analyzed a cohort of human

tissue samples comprising primary tumors ($n = 40$) and paired adjacent normal tissues ($n = 40$) from patients with MSS or MSI CRC (Fig. 1A). The detailed information of the clinical cohort is listed in Table S1. We performed

(See figure on previous page.)

Fig. 1 Tumor metabolic heterogeneity between patients with MSS and MSI CRCs. **(A)** Schematic illustration of untargeted metabolomics analysis of tissue samples ($n=80$) from patients with MSS ($n=20$) and MSI CRCs ($n=20$). **(B)** Metabolite classes of identified metabolites in MSS and MSI CRC tissues. **(C)** Partial least squares (PLS) shows different metabolic profiles among four sample groups. Each dot represents the averaged value from the analysis method. **(D)** Hierarchical clustering analyses using the top 50 dysregulated metabolites between CRC tumors and adjacent controls, as well as MSS and MSI tumors. Statistics were analyzed by one-way ANOVA. **(E)** Pathway enrichment analysis using significantly changed metabolites between groups. The pathway enrichment analysis was conducted using MetaboAnalyst. **(F-H)** Levels of SAM **(F)**, SAH **(G)** and SAM/SAH ratio **(H)** in patients with MSS CRC ($n=20$) and adjacent normal tissue controls ($n=20$), MSI CRC ($n=20$) and adjacent normal tissue controls ($n=20$). Data are shown as mean \pm SEM. Statistics were analyzed by two-sided Student's *t*-test. * $p < 0.05$, ** $p < 0.01$, *** $p < 0.001$, and **** $p < 0.0001$. A value of $p < 0.05$ was considered statistically significant

LC-MS-based untargeted metabolomics on these tissue samples, quantifying 595 metabolites for subsequent statistical analyses (Fig. 1B, Fig. S1A and Supplementary Data 1). The multivariate statistical analyses of the metabolomics data revealed profound differences in the tissue metabolome between CRC tumors and paired adjacent controls, as well as MSS and MSI tumors (Fig. 1C and Fig. S1B-D). Subsequent univariate analysis showed that 195, 114, 81 metabolites were significantly changed between MSS tumor and paired control, MSI tumor and paired control, MSS tumor and MSI tumor, respectively (fold change ≥ 1.2 or ≤ 0.83 , FDR adjusted $P < 0.05$, Fig. S1E-G). Hierarchical clustering analyses (HCA) using the top 50 dysregulated metabolites disclosed three different clusters among the groups as showed in Fig. 1D. Further pathway enrichment analysis revealed that multiple pathways were dysregulated in CRC tumors such as galactose metabolism, biosynthesis of unsaturated fatty acids, and distinct metabolism of carbohydrates (Fig. 1E). Specifically, MSS and MSI CRCs differed in metabolic pathways including glycerophospholipid metabolism, sphingolipid metabolism, cysteine and methionine metabolism, nicotine and nicotinamide metabolism, and carbohydrate metabolism.

MSS and MSI CRCs differ in SAM/SAH metabolism and T-cell signatures

Closer examination disclosed specific differences between MSS and MSI CRCs in critical metabolic intermediates in the SAM/SAH metabolism. In this pathway, SAM is synthesized from methionine through an adenosyl group transfer reaction catalyzed by the enzyme methionine adenosyltransferase (MAT) (Fig. S2A). The biosynthesis cycle forms either through SAH or methylthioadenosine (MTA). When compared to paired normal tissues stratified by microsatellite status, SAM was upregulated in MSS CRC but showed no changes in MSI CRCs (Fig. 1H). Intermediates including SAH and MTA were upregulated in both MSS and MSI CRCs (Fig. 1G, Fig. S2B). Interestingly, we found that MSS tumors displayed significantly higher levels of SAM, SAH, and MTA than those in MSI tumors. In addition, the ratio of SAM/SAH was significantly higher in MSS tumors than that in MSI tumors (Fig. 1H). Above differences between MSS

and MSI CRCs were not observed for methionine levels (Fig. S2C).

To further investigate the association between SAM/SAH metabolism with microsatellite status in CRC, we carried out additional analyses of gene expression data for an independent cohort ($n=144$) from the Gene Expression Omnibus database (GSE39582), which includes primary tumors collected from patients with MSS and MSI CRCs. The detailed information of the cohort is provided in Table S2. Albeit distinct changing trends of specific genes with isoforms, the results revealed profound differences in the synthesis and metabolism of SAM and SAH at the gene expression level between MSS and MSI CRCs (Fig. S2D). For examples, levels of *MAT2A* and *MAT2B* that express the enzyme catalyzing synthesis of SAM were significantly higher in MSI CRC than that in MSS CRC. For genes responsible for SAH production, lower expression of *DNMT1* while higher expression of *DNMT3A* were observed in MSS CRC than that in MSI CRC. The combined data demonstrated that MSS and MSI CRCs have prominent differences in SAM and SAH metabolism, at the levels of both metabolite biosynthesis and gene expression.

Furthermore, we computed the immune-related gene characteristics of the GSE39582 cohort to evaluate the abundance of immune cell infiltration in MSS and MSI. The immune-related gene characteristics were calculated using the single-sample gene-set enrichment analysis (ssGSEA) algorithm [32, 33]. The results showed that MSS CRC exhibit significantly lower levels of signatures associated with immune cells and immune responses than MSI CRC (Fig. 2A). Specifically, we observed that MSS CRC displayed lower T-cell signatures which are represented by CD8⁺ T cell, 13 T-cell signatures, and T-cell as showed in Fig. 2B-D. Moreover, we analyzed an additional public transcriptomic dataset (TCGA-COAD) for correlations between SAM metabolism genes and CD8⁺ T cell activity in MSS CRC ($n=270$). In the TCGA-COAD cohort, 26 genes associated with CD8⁺ T cell activation were chosen for correlation analyses with SAM metabolism genes (*MAT2A*, *MAT2B*, *DNMT1*, *DNMT3A*, *DNMT3B*, *GNMT*). In MSS CRC, we observed 68 significantly positive correlations between SAM metabolism genes and CD8⁺ T cell activity genes (Fig. 2E, $R > 0.5$ and p value < 0.05 , Pearson correlation). For examples,

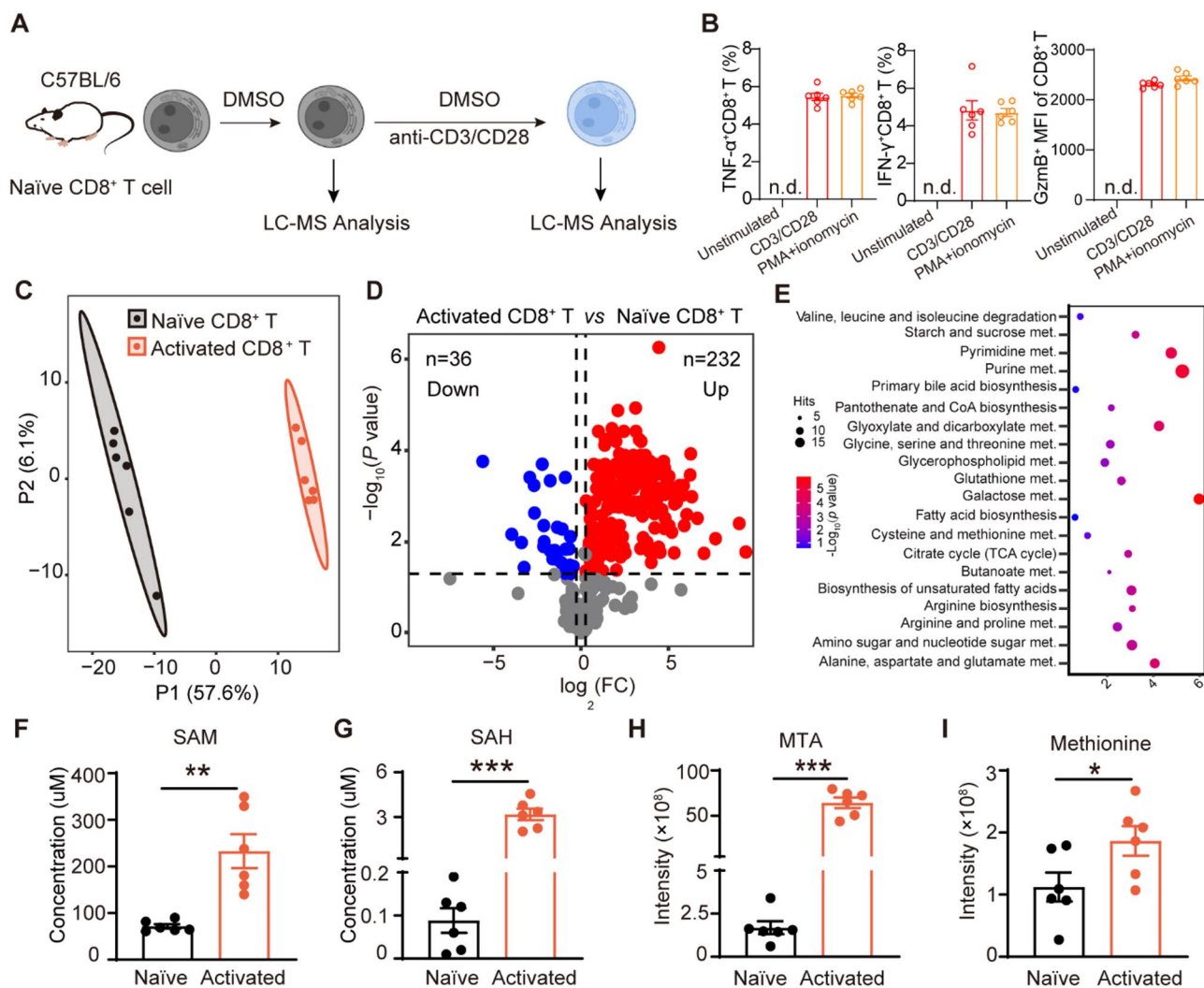


Fig. 3 Activated CD8⁺ T cells display enhanced SAM and SAH metabolism. **(A)** Schematic illustration of untargeted metabolomics analyses of naïve CD8⁺ T cells and activated CD8⁺ T cells from the spleen of C57BL/6 mice. **(B)** Levels of TNF- α , IFN- γ , GzmB⁺ among CD8⁺ T cells treated with solvent control (DMSO) in unstimulated naïve cells, under stimulation with CD3 and CD28 antibodies, and phorbol 12-myristate 13-acetate (PMA) and ionomycin for 72 h ($n=6$). **(C)** Partial least squares analysis shows distinct metabolic profiles between naïve and activated CD8⁺ T cells ($n=6$). **(D)** Volcano plots shows differential metabolites between naïve and activated CD8⁺ T cells. Red dots ($n=232$) and blue dots ($n=36$) represent metabolites that were increased and decreased in activated CD8⁺ T cells, respectively. **(E)** Pathway enrichment analysis using significantly changed metabolites ($n=268$). **(F-I)** Levels of SAM **(F)**, SAH **(G)**, MTA **(H)** and methionine **(I)** in naïve and activated CD8⁺ T cells ($n=6$). Data are shown as mean \pm SEM. Statistics were analyzed by two-sided Student's t -test. * $p < 0.05$, ** $p < 0.01$, *** $p < 0.001$, and **** $p < 0.0001$. A value of $p < 0.05$ was considered statistically significant

These results showed an enhanced SAM and SAH metabolism in the activated CD8⁺ T cells of mice.

SAM and SAH enhance the initial activation and effector function of CD8⁺ T cells

We next investigated the effects of SAM and SAH on mouse primary CD8⁺ T cells. Quantitative measurement of CD8⁺ T cells using LC-MS showed that the intracellular concentrations for SAM and SAH were approximately 84 μM and 0.04 μM , respectively (Fig. S4A, B). First, CD8⁺ T cells were isolated from spleens of wild-type C57BL/6 mice (6 weeks). Then, isolated CD8⁺ T cells were cultured with SAM or SAH under stimulation

with CD3 and CD28 treatment, followed by flow cytometry analyses (Fig. 4A and Fig. S4C). The results showed that both SAM and SAH treatment resulted in increased expressions of surface marker CD69 in CD8⁺ T cells ($n=6$, $P < 0.05$) (Fig. 4B, C), whereas no significant effects were observed on CD44 and CD25 expression (Fig. S4D-G). Therefore, both SAM and SAH enable to enhance the initial phase activation of CD8⁺ T cells. Moreover, both SAM and SAH increased levels of TNF- α , IFN- γ , and GzmB expression in anti-CD3/CD28-stimulated primary CD8⁺ T cells (Fig. 4D-I), suggesting the enhanced effector functions of CD8⁺ T cells. In addition, we assessed the effects of metabolite quantity and found that high

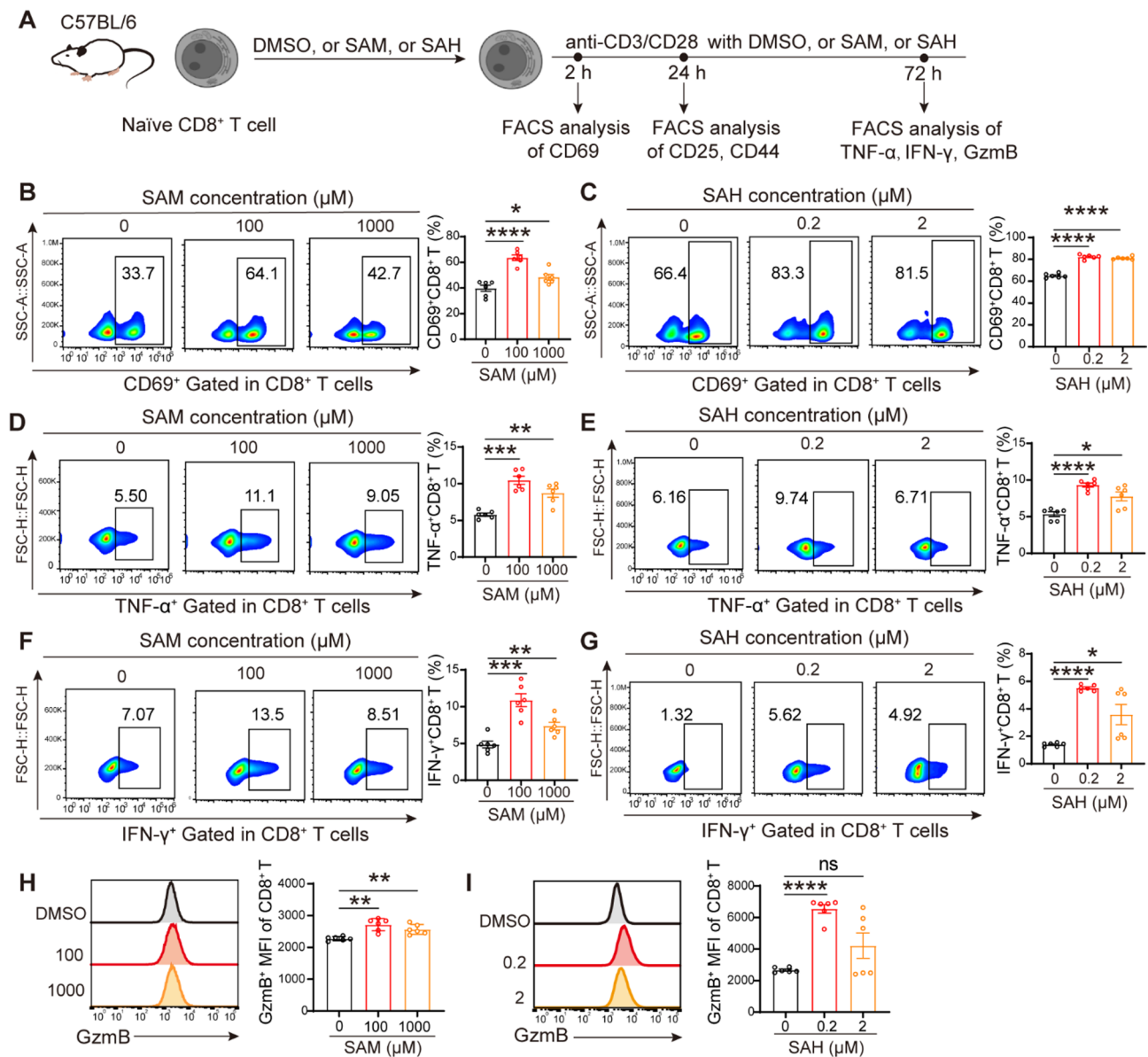


Fig. 4 SAM and SAH enhanced the initial activation and effector function of CD8⁺T cells. **(A)** Schematic procedure: splenic CD8⁺ T cells from C57BL/6 mice were treated with SAM or SAH or DMSO control for 48 h. Then, the CD8⁺ T cells were stimulated with CD3 and CD28 antibodies. The CD69⁺ of CD8⁺ T cells were quantified by FACS after 2 h; the CD25⁺ and CD44⁺ of CD8⁺ T cells were quantified by FACS after 24 h; the TNF-α⁺, IFN-γ⁺ and GzmB⁺ of CD8⁺ T cells were quantified by FACS after 72 h. **(B-C)** Effects of SAM **(B)** or SAH **(C)** on the percentage of CD69⁺ cells among CD8⁺ T cells ($n=6$). **(D-E)** Effects of SAM **(D)** or SAH **(E)** on the percentage of TNF-α⁺ cells among CD8⁺ T cells ($n=6$). **(F-G)** Effects of SAM **(F)** or SAH **(G)** on the percentage of IFN-γ⁺ cells among CD8⁺ T cells ($n=6$). **(H-I)** Effects of SAM **(H)** or SAH **(I)** on the percentage of IFN-γ⁺ cells among CD8⁺ T cells ($n=6$). MFI, mean fluorescence intensity. Data are shown as mean ± SEM. Statistics are analyzed by two-sided Student's *t*-test. ns, not significant, * $p < 0.05$, ** $p < 0.01$, *** $p < 0.001$, and **** $p < 0.0001$. A value of $p < 0.05$ was considered statistically significant

concentration of metabolites does not further promote production of activation and effector molecules (Fig. 4B-I). Collectively, these results demonstrated that SAM and SAH enhance the activation and effector function of CD8⁺ T cells upon stimulation.

Given that SAM is a methylation donor, we next investigate the impacts of SAM level on gene expression changes in CD8⁺ T cells. FIDAS-5 is an inhibitor of MAT2A which is the enzyme responsible for

SAM synthesis. To identify gene expression changes in response to MAT2A inhibition, naïve CD8⁺ T cells from mice were first activated by anti-CD3/CD28 treatment, then treated with FIDAS-5 for 48 h. LC-MS analysis of CD8⁺ T cells revealed that MAT2A inhibition by FIDAS-5 decreased cellular SAM level significantly (Fig. S5A). We next performed RNA-seq analysis on FIDAS-5 treated CD8⁺ T cells compared to controls. Results showed that 305 genes were significantly changed (FDR

adjusted $p < 0.05$), including 270 downregulated and 35 upregulated genes upon SAM depletion (Fig. S5B). Gene set enrichment analysis (GSEA) further revealed that top-ranked gene sets of regulation of cell activation, response to external stimulus and immune system processes were altered by SAM depletion (Fig. S5C). In particular, genes such as Cd86, Cd68, Cd72, Il1 α , Tnfrsf9, and Tnfrsf21 were significantly decreased upon SAM depletion (Fig. S5D-5I). Combined, these results showed that SAM depletion in T cells directly lead to impaired methylation and gene expression changes and suggest the SAM-mediated gene expression effects on CD8⁺ T cell functions.

Cancer cells outcompete CD8 T cells for SAM and SAH availability to impair T cell survival

Tumor progression and anti-tumor immune responses are shaped by the local microenvironment, wherein metabolite nutrients serve as a crucial niche. Nutrient

availability in the environment influences both tumor cell proliferation and immune cell survival and function [16, 18]. Next, we sought to examine whether tumor cells affect CD8⁺ T cell function through the availability of SAM and SAH in the microenvironment. We co-cultured two types of colon cancer cells (CT26 or MC38) and activated mouse CD8⁺ T cells for 48 h in a Transwell system which was used to mimic the tumor microenvironment (Fig. 5A). The apoptosis marker annexin V was examined for both CD8⁺ T cells and colon cancer cells.

First, we investigated the effects of SAM and SAH on apoptosis in CD8⁺ T cells that being cultured alone. Results showed that SAM reduced the apoptosis of CD8⁺ T cells, with a reduction proportion of 19.8% (Fig. 5B). Similar effect was observed for SAH treatment, with apoptotic CD8⁺ T cells being reduced by 15.5% (Fig. 5C). By contrast, the proportion of apoptotic CD8⁺ T cells was doubled when cocultured with colon cancer cells (CT26 and MC38) in the presence of SAM (Fig. 5D, E). Similar

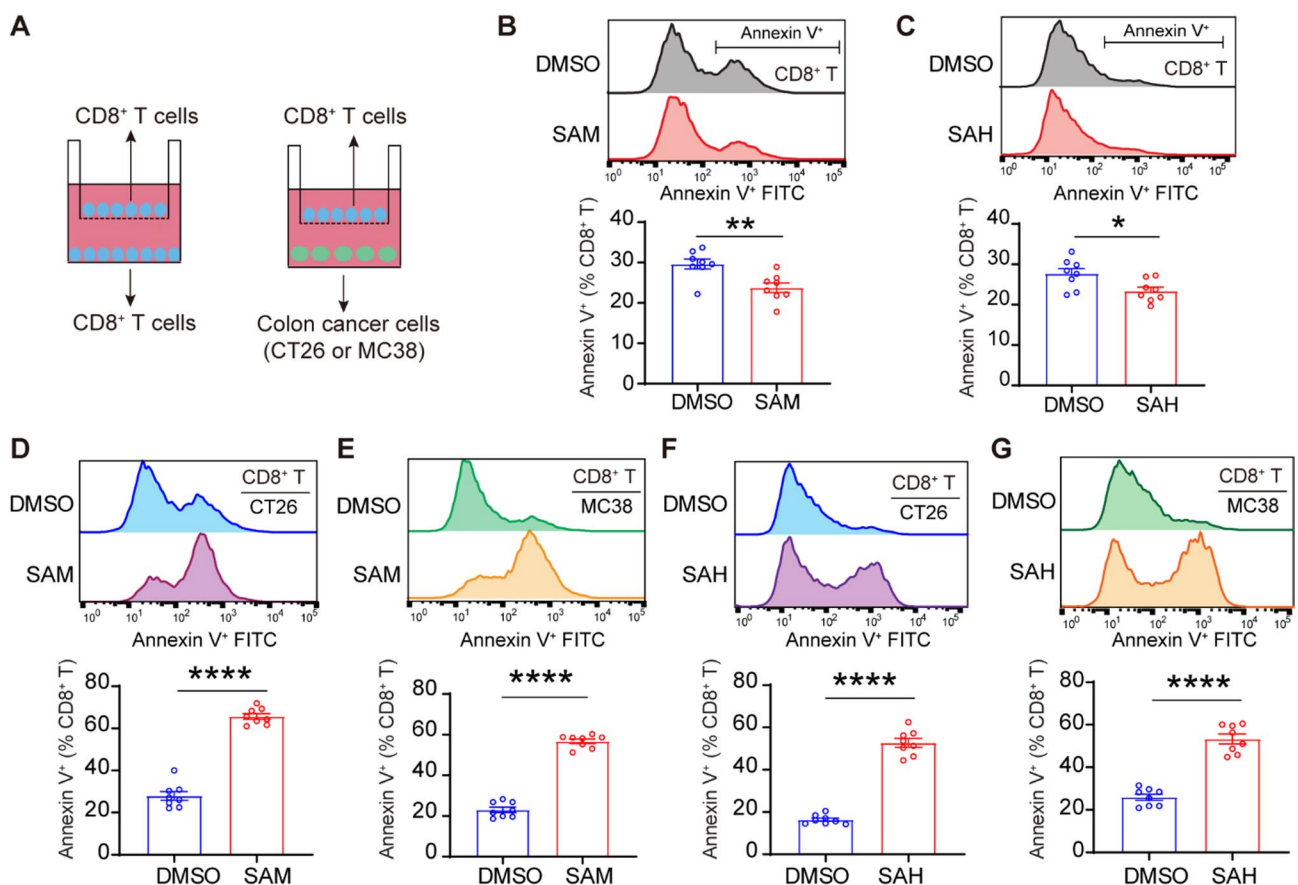


Fig. 5 Effects of SAM and SAH on CD8⁺T cell cocultured with colon cancer cells. (A) Schematic illustration of colon cancer cell and T cell co-culture in the Transwell system. (B-C) Apoptosis of CD8⁺ T cells under SAM (B) and SAH (C) treatment ($n = 8$). (D-E) Apoptosis of CD8⁺ T cells induced by SAM competition with CT26 cells (D) and MC38 cells (E). Colon cancer cells and activated CD8⁺ T cells were co-cultured for 48 h in a Transwell system with 100 μ M SAM ($n = 8$). (F-G) Apoptosis of CD8⁺ T cells induced by SAH competition with CT26 cells (F) and MC38 cells (G). Colon cancer cells and activated CD8⁺ T cells were co-cultured for 48 h in a Transwell system with 0.2 μ M SAH ($n = 8$)

Data are shown as mean \pm SEM. Statistics are analyzed by two-sided Student's t -test. * $p < 0.05$, ** $p < 0.01$, *** $p < 0.001$, and **** $p < 0.0001$. A value of $p < 0.05$ was considered statistically significant

increases in CD8⁺ T cell apoptosis were found for the addition of SAH in the co-culture system (Fig. 5E, G). We also measured the apoptosis of cancer cells in the same experiments. However, no changes were observed in annexin V expression for the cocultured CT26 and MC38 cancer cells (Fig. S6). These results showed that cocultured colon cancer cells in the presence of SAM and SAH cause apoptosis of CD8⁺ T cells but minimal effects on cancer cells.

In addition, we quantified cellular levels of SAM and SAH within CD8⁺ T cells and tumor cells for parallel experiments using LC–MS analysis. When CD8⁺ T cells were cultured alone, SAM and SAH supplementation increased the cellular metabolite levels of CD8⁺ T cells (Fig. S7A and S7B). When CD8⁺ T cells were cocultured with tumor cells under DMSO conditions, competition for SAM and SAH between CD8⁺ T cells and tumor cells is unlikely since the absent of SAM and SAH in the environment. This is also supported by the comparable levels of SAM and SAH in CD8⁺ T cells cultured alone and cocultured with cancer cells under DMSO conditions (Fig. S7A and S7B). By contrast, when SAM or SAH was supplemented to culture medium, cellular levels of SAM and SAH in the co-cultured CD8⁺ T cells were significantly lower than cells cultured alone because that tumor cells were out competing the T cells for SAM and SAH. Importantly, SAM and SAH levels within the CD8⁺ T cells in the SAM and SAH supplemented conditions were significantly lower than that in the DMSO conditions (Fig. S7A and S7B). In contrast to CD8⁺ T cells, cocultured tumor cells in the SAM and SAH supplemented conditions had significantly higher SAM/SAH levels than that in the DMSO conditions (Fig. S7C and S7D). Collectively, these data supported the proposed mechanism that tumor cells may outcompete CD8⁺ T cells for SAM and SAH availability in the environment to impair T cell function.

SAM improves T cell immunity and reduces tumor growth in mice

To investigate the *in vivo* effects of SAM and SAH on T cell immunity and tumor progression, we next conducted the LC–MS based metabolomics analysis and T cell analysis and of the MSS CRC tumor-bearing mice. We established a subcutaneous CT26 transplant mouse model (BALB/c) and treated tumors with PBS, SAM, or SAH 6 days after implantation ($n = 8$ in each group). Tumor, serum, spleen, and draining lymph node (dLN) samples were collected for subsequent LC–MS and flow cytometry analyses to examine metabolite levels and T cell populations (Fig. 6A). Quantitative LC–MS measurement revealed that SAM supplementation increased the levels of SAM both in tumor and serum of mice (Fig. S8A, B). Increased SAH in tumor but not in serum was observed

in mice with SAH supplementation (Fig. S8C, D). Tumor measurement showed that SAM, but not SAH, markedly reduces tumor growth in terms of tumor size and tumor weight (Fig. 6B–D and Fig. S8E). LC–MS based untargeted metabolomics revealed distinctive metabolic profiles among control, SAM or SAH treated tumors (Fig. S8F). Univariate analysis showed that a total of 209 and 132 tumor metabolites were significantly changed (fold change ≥ 1.2 or ≤ 0.83 , FDR adjusted $P < 0.05$) induced by SAM and SAH treatment, respectively (Fig. S8G–I). These dysregulated metabolites were enriched in metabolic pathways such as nicotinate and nicotinamide metabolism, and nucleotide metabolism (Fig. S8J).

Flow cytometry analyses revealed that SAM significantly increased CD4⁺ T cell population in tumor-infiltrating lymphocytes and improved the proliferation of CD4⁺ T cells as an increased Ki67⁺CD4⁺ population being observed (Fig. 6E, F, and Fig. S9). In addition, SAM increased FOXP3⁺CD4⁺ regulatory T (T_{reg}) cell population (Fig. 6G). Importantly, SAM elevated the percentages of CD8⁺ T cells as a fraction of the CD45⁺ leukocytes infiltration in CT26 tumors and promoted the proliferation of CD8⁺ T cells (Fig. 6H–I). SAM supplementation had no effects on CD4⁺ and CD8⁺ T cell populations in spleen and dLNs (Fig. S10). In particular, we found that SAM treatment results in a lower percentage of PD-1⁺CD8⁺ T cells compared to controls (Fig. 6J). Further examination of the exhausted status of tumor-infiltrating T cells revealed that SAM significantly reduced both initial and terminal exhaustion of CD8⁺ T cells in tumors, as indicated by decreased proportions of PD-1⁺Tim-3⁻CD8⁺ T cells and PD-1⁺Tim-3⁺CD8⁺ T cells compared to controls (Fig. 6K). As such, SAM supplementation increased the expression of TNF- α , IFN- γ in CD8⁺ T cells, suggesting an enhanced cytokine production (Fig. 6L, M).

Investigation of the *in vivo* effects of SAH on T cell immunity showed that SAH increased the population and proliferation of CD4⁺ T cells in tumor-infiltrating lymphocytes (Fig. S11A, B). However, SAH supplementation had no effects on FOXP3⁺CD4⁺ regulatory T (T_{reg}) cell population (Fig. S11C). With regard to the effects on CD8⁺ T cells, SAH elevated the CD8⁺ T cell population in CT26 tumors and promoted the proliferation (Fig. S11D, E). Effects on PD-1⁺CD8⁺ T cell population were not observed in tumor-infiltrating CD8⁺T cells of mice supplemented with SAH (Fig. S11F). SAH promoted the initial exhaustion though it reduced the terminal exhaustion of CD8⁺ T cells (Fig. S11G). In addition, no significant immune-enhancement effects were observed with the SAH treatment in the tumor-bearing mice (Fig. S11H, I).

Collectively, these data demonstrated that SAM promotes proliferation and decreases exhaustion of the tumor-infiltrating CD8⁺ T cells towards improved T cell

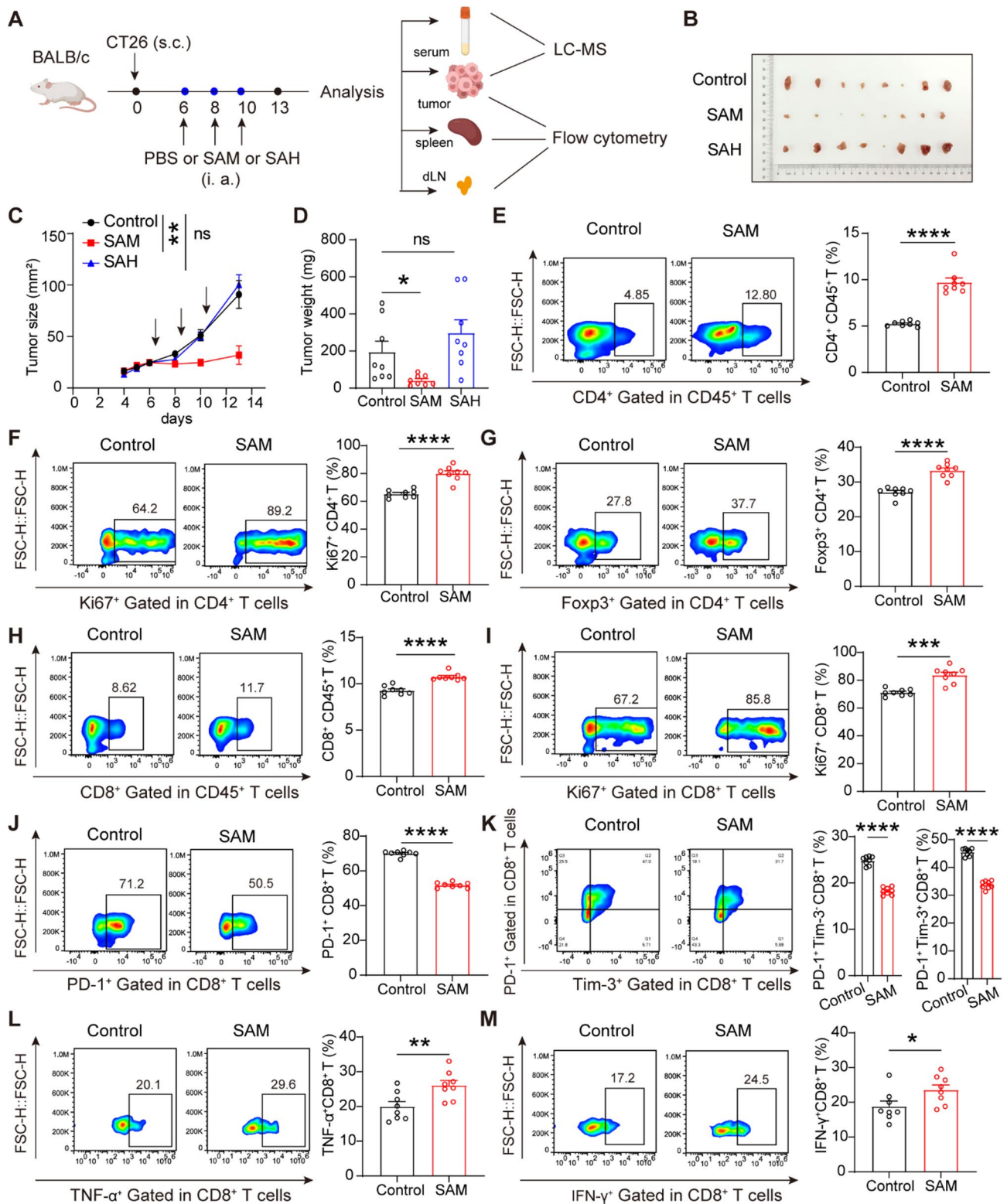


Fig. 6 Effects of SAM and SAH on T cell function and tumor growth in vivo. **(A)** Schematic experimental procedures: WT mice (BALB/c) were treated with PBS or SAM or SAH through intratumoral administration (i.a.) 6 days after implantation subcutaneously (s.c.) with CT26 cells. **(B-D)** Representative tumor images **(B)**, tumor growth curves **(C)**, and tumor weight **(D)** at 13 days after inoculation with CT26 cell; $n=8$. **(E-M)** Representative flow cytometry plots of $CD4^+CD45^+$ **(E)**, $Ki67^+CD4^+$ **(F)**, $Foxp3^+CD4^+$ **(G)**, $CD8^+CD45^+$ **(H)**, $Ki67^+CD8^+$ **(I)**, $PD-1^+CD8^+$ **(J)**, $PD-1^+Tim-3^+CD8^+$ T and $PD-1^+Tim-3^+CD8^+$ T **(K)**, $TNF-\alpha^+CD8^+$ **(L)**, $IFN-\gamma^+CD8^+$ **(M)** among the tumor-infiltrating leukocyte cells in CT26 tumor-bearing mice treated with SAM. $n=8$. Data are shown as mean \pm SEM. Statistics are analyzed by two-sided Student's *t*-test. ns, not significant, * $p < 0.05$, ** $p < 0.01$, *** $p < 0.001$, and **** $p < 0.0001$. A value of $p < 0.05$ was considered statistically significant

immunity and reduced tumor progression in the MSS CRC tumor-bearing mice.

Discussion

The intrinsic complexity and heterogeneity between patients with MSS and MSI CRCs present difficulties in colorectal cancer treatment, with significant differences in treatment plans, treatment outcomes, prognosis, and survival rates among different individuals. Spurred by advanced mass spectrometry based metabolomic technologies, untargeted metabolomics allows the colorectal cancer metabolism to be investigated in a so far unprecedented depth. Metabolic milieu is increasingly recognized as a salient feature which influences colon tumor development, therapeutic effects, and prognosis [25]. However, to date, there have been no studies investigating tumor-intrinsic metabolic differences between patients with MSS and MSI CRCs. In this study, we disclosed metabolic heterogeneity between MSS and MSI CRCs including cysteine and methionine metabolism, nicotinate and nicotinamide metabolism, and carbohydrate metabolism. Particularly, we discovered that MSS and MSI CRCs differ in SAM and SAH metabolism, and further demonstrated that SAM can enhance CD8⁺ T cell function in vitro and in vivo. This is a unique study to show a SAM and SAH metabolism-enhanced metabolic subphenotype in patients with MSS CRCs, with implications for anti-tumor immunity and immunotherapeutic outcomes in CRC.

The metabolite milieu such as arginine, lactate, methionine, taurine, and microbial metabolite indole-3-propionic acid, can simultaneously regulate both tumor cells and immune cells, thereby having significant impacts on cancer immunotherapy [16, 18, 34–36]. More importantly, tumor cells are highly metabolically active and outcompete T cells for essential metabolite nutrients in the tumor microenvironment. For examples, intensive amino acid consumption by tumor cells cause arginine, taurine, and methionine deficiencies in T cells, impairing CD8⁺ T cell immunity against tumor progression. S-adenosylmethionine, which is synthesized via the methionine cycle, has been shown to inhibit certain tumors such as breast and liver cancers, as well as colon cancer cells [37]. In the patient cohort, we identified that MSS tumors had significant higher levels of SAM and SAH than MSI tumors. Analysis of the GSE39582 transcriptomic dataset demonstrated the differences in SAM metabolism between MSS and MSI CRCs at the gene expression level. Unlike the levels of SAM and SAH, the gene expression data shows that the expression of MAT2A and MAT2B are higher in the MSI tumors compared to the MSS tumors. This can be explained by the fact that the gene expression level does not always correlate with protein level. In particular for metabolic enzymes, the protein

levels and enzymatic activities are largely impacted by post-translational modification, substrate availability and the finely tuned metabolic network. Therefore, the levels of end-products catalyzed by metabolic enzymes are not always consistent with gene expression. Combined, we proposed a mechanism of how MSS tumors are obtaining higher SAM levels due to altered MAT2A/B gene expression. Although there has been limited reports on metabolic heterogeneity between MSS and MSI CRCs, given the profound impacts of SAM availability on DNA and histone methylation, the distinctive SAM metabolism may explain the link between tumor mutational burden and immunotherapeutic outcomes in patients with MSS CRC compared to MSI CRC.

Another key aspect of the current study was to assess the effects of SAM and SAH on CD8⁺ T cell function in vitro and in vivo. Our results showed that both SAM and SAH can enhance the activation and effector function of CD8⁺ T cells upon stimulation in vitro. Metabolic effects downstream of SAM and SAH may be involved, such as improved anti-oxidant capacity due to GSH synthesis. But in vivo system in the tumor-bearing mice, no significant immune-enhancement effects were observed with the SAH treatment. This may be due to the presence of large amounts of reactive oxygen species in the tumor environment, and SAH is not sufficiently effective through GSH action alone to combat oxidative stress. SAM is the key methylation donor for epigenetic regulation. Bian et al. recently demonstrated that tumor cells outcompeted T cells for methionine, thereby lowering intracellular level of the synthesized SAM and resulting in loss of dimethylation of H3K79me2 in CD8⁺ T cells with impaired immunity. Consistently, we found that lowering intracellular SAM results in changes in gene expression in CD8⁺ T cells, in particular for genes associated with cell activation and immune system processes such as Cd86, Cd68, Cd72, Il1 α , Tnfrsf9, and Tnfrsf21. Combined with the in vivo data that SAM promotes proliferation and decreases exhaustion of the tumor-infiltrating CD8⁺ T cells towards improved immunity and reduced tumor progression in the tumor-bearing mice, it suggests that SAM orchestrates gene expression towards CD8⁺ T cell functions.

Conclusions

In this study, we analyzed a cohort of tissue samples from patients with CRCs using comprehensive untargeted metabolomics. We successfully identified that MSS and MSI CRCs differ in SAM and SAH metabolism. Specifically, we demonstrated that SAM and SAH enhance the initial activation and effector function of CD8⁺ T cells. Colon cancer cells outcompete CD8⁺ T cells for SAM and SAH availability to impair T cell survival. SAM treatment promotes the T cell proliferation and reduces exhaustion

of the tumor-infiltrating CD8⁺ T cells, with a result of suppressed tumor growth in the MSS CRC tumor-bearing mice. Our work uncovers a SAM and SAH metabolism-enhanced metabolic subphenotype in patients with MSS CRC, with potential application of metabolic modulation of T cell functions tailored for MSS CRC immunotherapy.

Supplementary Information

The online version contains supplementary material available at <https://doi.org/10.1186/s40170-025-00394-2>.

Supplementary Material 1: Supplemental Data 1. Metabolomics data of tissue samples from patients with MSS or MSI CRCs

Supplementary Material 2: Document S1. Figures S1-S11 and Tables S1-S3

Acknowledgements

We thank the instructive supports of Zhengxu Ren and Dr. Chenqi Xu from the Center for Excellence in Molecular Cell Science, Chinese Academy of Sciences for flow cytometry analysis. We thank Dr. Nan Liu from Interdisciplinary Research Center on Biology and Chemistry for RNA-seq analysis.

Author contributions

Y.C. and Z.J.Z. conceived the idea and designed the experiment. X.Y. conducted the cell and animal experiments and analyzed the data. X.Y., and T.K. conducted the metabolomic sample preparation, data acquisition, data processing and data analysis. H.W. helped the data analysis. J.Z. contributed the clinical samples. Y.C. drafted the manuscript. All authors read and approved the final manuscript. Y.C. supervised the project.

Funding

This study was supported by the National Natural Science Foundation of China (32201211) and Shanghai Key Laboratory of Aging Studies (19DZ2260400), Shanghai Municipal Science and Technology Major Project, and Shanghai Basic Research Pioneer Project.

Data availability

The metabolomics data with raw LC-MS data files generated in this study have been deposited in the National Omics Data Encyclopedia (<https://www.biosin.org/node>) under the accession code OEP00006137.

Declarations

Competing interests

The authors declare no competing interests.

Received: 17 January 2025 / Accepted: 9 May 2025

Published online: 19 May 2025

References

1. Evrard C, Tachon G, Randrian V, Karayan-Tapon L, Tougeron D. Microsatellite instability: diagnosis, heterogeneity, discordance, and clinical impact in colorectal Cancer. *Cancers*. 2019;11(10):1567.
2. Bai Y, Li T, Wang Q, You W, Yang H, Xu X, Li Z, Zhang Y, Yan C, Yang L, et al. Shaping immune landscape of colorectal cancer by cholesterol metabolites. *EMBO Mol Med*. 2024;16(2):334–60.
3. Smyrk TC, Watson P, Kaul K, Lynch HT. Tumor-infiltrating lymphocytes are a marker for microsatellite instability in colorectal carcinoma. *Cancer*. 2001;91(12):2417–22.
4. Lumish MA, Cercek A. Immunotherapy for the treatment of colorectal cancer. *J Surg Oncol*. 2021;123(3):760–74.
5. Picard E, Verschoor CP, Ma GW, Pawelec G. Relationships between immune landscapes, genetic subtypes and responses to immunotherapy in colorectal cancer. *Front Immunol*. 2020;11:369.
6. Anderson NM, Simon MC. The tumor microenvironment. *Curr Biol*. 2020;30(16):R921–5.
7. de Visser KE, Joyce JA. The evolving tumor microenvironment: from cancer initiation to metastatic outgrowth. *Cancer Cell*. 2023;41(3):374–403.
8. Elia I, Haigis MC. Metabolites and the tumour microenvironment: from cellular mechanisms to systemic metabolism. *Nat Metabolism*. 2021;3(1):21–32.
9. Arner EN, Rathmell JC. Metabolic programming and immune suppression in the tumor microenvironment. *Cancer Cell*. 2023;41(3):421–33.
10. Wang Y, Wang F, Wang L, Qiu S, Yao Y, Yan C, Xiong X, Chen X, Ji Q, Cao J, et al. NAD(+) supplement potentiates tumor-killing function by rescuing defective TUB-mediated NAMPT transcription in tumor-infiltrated T cells. *Cell Rep*. 2021;36(6):109516.
11. Fowle-Grider R, Rowles JL, Shen I, Wang Y, Schwaiger-Haber M, Dunham AJ, Jayachandran K, Inkman M, Zahner M, Naser FJ, et al. Dietary Fructose enhances tumour growth indirectly via interorgan lipid transfer. *Nature*. 2024;636(8043):737–44.
12. Pavlova Natalya N, Thompson Craig B. The emerging hallmarks of Cancer metabolism. *Cell Metabol*. 2016;23(1):27–47.
13. Loftus RM, Finlay DK. Immunometabolism: cellular metabolism turns immune regulator**. *J Biol Chem*. 2016;291(1):1–10.
14. Wang A, Luan HH, Medzhitov R. An evolutionary perspective on immunometabolism. *Science*. 2019;363(6423):eaar3932.
15. Bacigalupa ZA, Landis MD, Rathmell JC. Nutrient inputs and social metabolic control of cell fate. *Cell Metabol*. 2024;36(1):10–20.
16. Geiger R, Rieckmann JC, Wolf T, Basso C, Feng Y, Fuhrer T, Kogadeeva M, Picotti P, Meissner F, Mann M, et al. L-Arginine modulates T cell metabolism and enhances survival and Anti-tumor activity. *Cell*. 2016;167(3):829–e842813.
17. Canale FP, Basso C, Antonini G, Perotti M, Li N, Sokolovska A, Neumann J, James MJ, Geiger S, Jin W, et al. Metabolic modulation of tumours with engineered bacteria for immunotherapy. *Nature*. 2021;598(7882):662–6.
18. Bian Y, Li W, Kremer DM, Sajjakulnukit P, Li S, Crespo J, Nwosu ZC, Zhang L, Czerwonka A, Pawlowska A, et al. Cancer SLC43A2 alters T cell methionine metabolism and histone methylation. *Nature*. 2020;585(7824):277–82.
19. Hao M, Hou S, Li W, Li K, Xue L, Hu Q, Zhu L, Chen Y, Sun H, Ju C, et al. Combination of metabolic intervention and T cell therapy enhances solid tumor immunotherapy. *Sci Transl Med*. 2020;12(571):eaaz6667.
20. Peng JJ, Wang L, Li Z, Ku CL, Ho PC. Metabolic challenges and interventions in CAR T cell therapy. *Sci Immunol*. 2023;8(82):eabq3016.
21. Johnson CH, Ivanisevic J, Siuzdak G. Metabolomics: beyond biomarkers and towards mechanisms. *Nat Rev Mol Cell Biol*. 2016;17(7):451–9.
22. Patti GJ, Yanes O, Siuzdak G. Metabolomics: the apogee of the omics trilogy. *Nat Rev Mol Cell Biol*. 2012;13(4):263–9.
23. Oresic M. Metabolomics, a novel tool for studies of nutrition, metabolism and lipid dysfunction. *Nutr Metab Cardiovasc Dis*. 2009;19(11):816–24.
24. Johnson Caroline H, Dejea Christine M, Edler D, Hoang Linh T, Santidrian Antonio F, Felding Brunhilde H, Ivanisevic J, Cho K, Wick Elizabeth C, Hechenbleikner Elizabeth M, et al. Metabolism links bacterial biofilms and Colon carcinogenesis. *Cell Metabol*. 2015;21(6):891–7.
25. Wang H, Jia H, Gao Y, Zhang H, Fan J, Zhang L, Ren F, Yin Y, Cai Y, Zhu J et al. Serum metabolic traits reveal therapeutic toxicities and responses of neoadjuvant chemoradiotherapy in patients with rectal cancer. *Nat Commun* 2022, 13(1).
26. Cai Y, Rattray NJW, Zhang Q, Mironova V, Santos-Neto A, Hsu K-S, Rattray Z, Cross JR, Zhang Y, Paty PB, et al. Sex differences in Colon cancer metabolism reveal A novel subphenotype. *Sci Rep*. 2020;10(1):4905.
27. Zhu J, Djukovic D, Deng L, Gu H, Himmati F, Chiorean EG, Raftery D. Colorectal Cancer detection using targeted serum metabolic profiling. *J Proteome Res*. 2014;13(9):4120–30.
28. Wang R, Yin Y, Li J, Wang H, Lv W, Gao Y, Wang T, Zhong Y, Zhou Z, Cai Y et al. Global stable-isotope tracing metabolomics reveals system-wide metabolic alternations in aging Drosophila. *Nat Commun* 2022, 13(1).
29. Shen X, Wang R, Xiong X, Yin Y, Cai Y, Ma Z, Liu N, Zhu ZJ. Metabolic reaction network-based recursive metabolite annotation for untargeted metabolomics. *Nat Commun*. 2019;10(1):1516.
30. Zhou Z, Luo M, Zhang H, Yin Y, Cai Y, Zhu Z-J. Metabolite annotation from knowns to unknowns through knowledge-guided multi-layer metabolic networking. *Nat Commun* 2022, 13(1).
31. Fan H, Xia S, Xiang J, Li Y, Ross MO, Lim SA, Yang F, Tu J, Xie L, Dougherty U, et al. Trans-vaccenic acid reprograms CD8(+) T cells and anti-tumour immunity. *Nature*. 2023;623(7989):1034–43.
32. Hänzelmann S, Castelo R, Guinney J. GSVA: gene set variation analysis for microarray and RNA-Seq data. *BMC Bioinformatics*. 2013;14(1):7.

33. Wang H, Zhou Y, Zhang Y, Fang S, Zhang M, Li H, Xu F, Liu L, Liu J, Zhao Q et al. Subtyping of microsatellite stability colorectal cancer reveals guanylate binding protein 2 (GBP2) as a potential immunotherapeutic target. *J Immunother Cancer* 2022, 10(4).
34. Peralta RM, Xie B, Lontos K, Nieves-Rosado H, Spahr K, Joshi S, Ford BR, Quann K, Frisch AT, Dean V, et al. Dysfunction of exhausted T cells is enforced by MCT11-mediated lactate metabolism. *Nat Immunol.* 2024;25(12):2297–307.
35. Cao T, Zhang W, Wang Q, Wang C, Ma W, Zhang C, Ge M, Tian M, Yu J, Jiao A, et al. Cancer SLC6A6-mediated taurine uptake transactivates immune checkpoint genes and induces exhaustion in CD8+T cells. *Cell.* 2024;187(9):2288–e23042227.
36. Jia D, Wang Q, Qi Y, Jiang Y, He J, Lin Y, Sun Y, Xu J, Chen W, Fan L, et al. Microbial metabolite enhances immunotherapy efficacy by modulating T cell stemness in pan-cancer. *Cell.* 2024;187(7):1651–e16651621.
37. Mahmood N, Arakelian A, Muller WJ, Szyf M, Rabbani SA. An enhanced chemopreventive effect of Methyl donor S-adenosylmethionine in combination with 25-hydroxyvitamin D in blocking mammary tumor growth and metastasis. *Bone Res* 2020, 8(1).

Publisher's note

Springer Nature remains neutral with regard to jurisdictional claims in published maps and institutional affiliations.